Nano Materials Science 2 (2020) 72–79

Contents lists available at ScienceDirect

Nano Materials Science

journal homepage: www.keaipublishing.com/cn/journals/nano-materials-science/

Revisiting anisotropy in the tensile and fracture behavior of cold-rolled 316L stainless steel with heterogeneous nano-lamellar structures

Zesheng You [a,*], Huangliu Fu [a], Shoudao Qu [a], Weikang Bao [a], Lei Lu [b,**]

[a] Herbert Gleiter Institute of Nanoscience, Nanjing University of Science and Technology, Nanjing, 210094, China
[b] Shenyang National Laboratory for Materials Science, Institute of Metal Research, Chinese Academy of Sciences, Shenyang, 110016, China

ARTICLE INFO

Keywords:
Heterogeneous nano-lamellar structure
Mechanical anisotropy
Fracture behavior
Specimen size effect
Strain path effect

ABSTRACT

We produced a 316L stainless steel with heterogeneous nanometer-thick lamellar structures by severe cold-rolling at room temperature, and conducted micro-scale tensile tests in different orientations to evaluate both the in-plane (parallel to the nano-lamellae) and out-of-plane (normal and 45° inclined to the nano-lamellae) mechanical anisotropy. The parallel orientation demonstrates the greatest tensile strength while the inclined orientation exhibits the least strength. The tensile tests in normal and inclined directions also indicate significant transient elastic-plastic response due to the strain path change. Fractographic examination demonstrates that the specimen fails in the normal direction by premature micro-void nucleation and growth, which restricts its tensile strength; however, we identified zig-zag cracking associated with lamellar shear cracking in the inclined direction.

1. Introduction

Nano-lamellar single-phase metals and multi-phase composites have received considerable attention recently owing to their appealing mechanical properties, such as high strength, enhanced thermal stability, promoted fatigue resistance and radiation damage tolerance [1–5]. The nano-lamellar structures can be generated by monotonic severe plastic deformation, such as high pressure torsion (HPT) [6], accumulative roll bonding (ARB) [7,8], cold rolling [9,10] and surface mechanical grinding [1,11], or alternatively by bottom-up techniques, including electro-deposition and magnetron sputtering [12,13]. The preferential alignment of the internal grain boundaries or phase interfaces unavoidably leads to significant anisotropy in various material properties. For example, the strengthening effect may substantially vary depending on the loading direction with respect to the lamellae [14,15]. Thus, it is important to perform systematic mechanical investigations in different stressing directions to quantify the magnitude of the plastic anisotropy and to determine the ways in which the underlying deformation mechanism depends on the loading direction.

However, constrained by finite specimen thicknesses, most mechanical evaluations currently available have been conducted parallel to the lamellar structures [16–18]. The out-of-plane mechanical measurements are rather scarce. Recently, this deficiency has been remedied practically by a rapid development in micro-mechanical evaluation techniques based on nano-indentations and micro-pillar compressions [19–21]. However, regarding the micro mechanical investigations, there are some ambiguities which must be clarified. First, the strengths from the microscale tests is not only related to the microstructural feature, but also constitutes a complicated function of the indenter or specimen size [22,23]. Second, although nano-indentation and micro compressions are advantageous for measuring strength, information on ductility and strain hardening is not directly accessible by such tests. Moreover, compressive stress suppresses the potential failure related to the laminated structures. Tensile tests must be conducted uniaxially in different directions to achieve a better understanding of the effect of lamellar directionality on the inherent tensile ductility and fracture behavior.

Previous researchers have conducted a series of tension experiments to investigate the mechanical behavior of cold-rolled 316L stainless steel (SS) consisting of nano-scale lamellar structures parallel to rolling plane [24–27]. Miura et al. have reported a significant in-plane mechanical anisotropy with strength in transverse direction much higher than in rolling direction [26]. However, there is still a lack of the out-of-plane mechanical tests necessary to determine the strength and tensile ductility when the nano-lamellae are normal or highly inclined to the stressing direction. In this study, we have carefully explored the tensile behaviors perpendicular, parallel, and 45° inclined to the lamellar

* Corresponding author.
** Corresponding author.
E-mail addresses: zsyou@njust.edu.cn (Z. You), llu@imr.ac.cn (L. Lu).

https://doi.org/10.1016/j.nanoms.2020.03.001

Available online 11 March 2020
2589-9651/© 2020 Chongqing University. Production and hosting by Elsevier B.V. on behalf of KeAi. This is an open access article under the CC BY-NC-ND license (http://creativecommons.org/licenses/by-nc-nd/4.0/).

structure, using micro specimens of over 50 μm thick and sufficiently large to eliminate the potential sample size effect We will also probe via fractographic examination the effect of loading direction on the tensile fracture process.

2. Experimental details

The material under investigation was a commercial ANSI 316L SS hot-rolled and thermally annealed to obtain equiaxed austenitic grains. The chemical composition of the material is given in Table 1. The material was deformed by cold rolling at room temperature to a final thickness of ~4 mm and a total thickness reduction of about 85%, corresponding to an effective true strain of ~2.2.

We conducted microscale tensile tests in different directions with respect to the rolling plane to probe the orientation dependence of the mechanical response of the cold-rolled sample. As schematically shown in Fig. 1a, we tested two in-plane directions, i.e., the rolling direction (RD) and the transverse direction (TD), as well as two out-of-plane directions, i.e., the normal direction (ND) and an inclined direction (ID). The ID was in the TD-ND plane and made an angle of 45° with the TD (Fig. 1a). The micro-tensile specimens were fabricated by a laboratory femtosecond laser micromachining system (FemtoLAB, Altechna, Lithuania). Due to the ultra-short pulse duration (~250 fs) of the laser beam, the material was removed before the heat energy was dissipated into surrounding material, thereby producing a negligible heat affected zone [28–31]. Cross-sectional slices with a thickness of ~500 μm were cut by electrical discharge machining, mechanically ground with successively finer SiC papers and then electrochemically polished to the target thickness (~50 μm) necessary for machining the dog-bone shape. The fabricated micro-specimens were further slightly electro-chemically polished to remove fabrication debris and any roughness of the cutting surface. Fig. 1b shows an optical micrograph of a high-quality micro--tensile specimen fabricated by this procedure. The specimen had a gauge width of 100 μm, a gauge length of 250 μm and a fillet radius of 50 μm.

The micro tensile tests were conducted on a custom-designed micro-mechanical testing instrument at room temperature. Before the tests, the micro tensile specimen was fixed to a sample holder using ethyl cyano-acrylate glue and carefully moved into a tungsten gripper via a two-axis motorized motion stage, as shown in Fig. 1c. The installation and alignment was monitored in both front and side views by two high resolution cameras. A piezo stepper linear actuator (N-381 NEXACT, Physik Instrumente) with a position resolution of 20 nm was used to load the specimen. The applied force was measured by a miniature tension/compression load cell (LCFD-1KG, Omega Engineering) with a capacity of 10 N and a resolution of about 15 mN. The strain in the gauge section was determined by digital image correlation (DIC) [32,33]. For this purpose, random black dots were sprayed onto the specimen surface by atomizing black ink, and several subsets of pixels were selected at both ends of the gauge section to calculate the extension, as shown in Fig. 1c. The tensile tests were displacement controlled with a displacement rate of 0.1 μm, corresponding to a nominal strain rate of 3×10^{-4} s^{-1}. For each direction, five specimens were tested in order to guarantee the reproducibility of the result.

For comparison, the tensile tests in the RD and TD were also conducted with macro specimens with a gauge length of 5 mm, a gauge section of 2×1 mm^2 (a proportional scale-up of the micro specimens). The macro tensile tests were performed on an Instron 5982 mechanical testing machine at room temperature with the same strain rate as the micro tensile tests. The gauge strain was also measured by a non-contact DIC strain gauge, as described in detail in Ref. [33].

Table 1
Chemical composition (wt%) of the 316L SS.

C	Mn	Si	P	S	Cr	Ni	Mo	Fe
0.022	1.29	0.37	0.04	0.055	16.64	11.09	2.0	Balance

The microstructure of the as-rolled 316L SS was characterized by an FEI Verios 460 field emission gun scanning electron microscope (FEG-SEM) and an FEI TECNAI G2 20 transmission electron microscope (TEM) operating at an accelerating voltage of 200 kV. The fracture surfaces were examined by an FEI Quanta 250 FEG-SEM. The phase composition was analyzed by X-ray diffraction (XRD) on a Bruker AXS D8 Advance diffractometer with Cu Kα radiation.

3. Results

3.1. Microstructure

Fig. 2 displays the cross-sectional microstructure of the cold rolled 316L SS inspected along the TD. The overall SEM micrograph in Fig. 2a demonstrates that the microstructure after severe cold rolling is rather heterogeneous. Magnified TEM observations (Fig. 2c) reveal that most regions are occupied by extremely elongated grains forming typical lamellae separated by planar boundaries which are either parallel to or deviate by small angles from the RD. The boundaries curve with a high density of accumulated dislocations. Statistical analysis indicates that the lamellar thickness λ ranges from 10 to 160 nm with a volume averaged value of 60 nm (Fig. 2d). Due to the low stacking fault energy of the 316L SS, both the dislocation behavior and deformation twinning act to control the rolling deformation and microstructural refinement. It is believed that twinning is the primary deformation mechanism which produces the nano-lamellae ($\lambda < 100$ nm) whereas the wide lamellae arise from an accumulation of dislocations and rotation of subdivided crystallites [34–36]. Deformation twinning takes place only in grains of favorable orientations, and the twins are gradually destructured by localized shear bands (Fig. 2b) to highly elongated grains that are progressively rotated towards the rolling plane with increasing rolling strain. Some bundles of deformation nanotwins, rhomboid in shape, remain within the lamellar structures, as shown in Fig. 2a and magnified in Fig. 2b. As roughly estimated, the nanotwin regions possess a volume fraction of 10–15%, fewer than that (~25%) in the 316L SS treated by dynamic plastic deformation due to the lower strain rate and larger applied strain [37]. TEM observations in Fig. 2e show many dislocations stored along the twin boundaries (TBs). The twin/matrix lamellar thickness is smaller than 100 nm, with a volume averaged value of about 30 nm. The XRD profile in Fig. 2f shows that, in addition to the major γ austenite phase, there are small peaks which belong to α' martensite phase, suggesting the occurrence of martensite transformation during cold rolling, as often identified for the 316L SS [38,39]. The volume fraction of the martensite phase is estimated to be about 15%.

3.2. Tensile properties

Fig. 3 shows the engineering stress–strain curves for the cold-rolled 316L SS tested using micro tensile specimens in four different directions. We plotted all the curves from the repeated tests for each direction on one graph to demonstrate the high reproducibility of the tests, and included representative curves (solid black line without symbols) obtained from the macro tensile tests in the RD and TD for comparison. Table 2 summarizes the derived mechanical properties, including 0.2% offset yield strength (σ_y), ultimate tensile strength (σ_{uts}), uniform elongation (δ_u), and fracture elongation (δ_f). Fig. 3a shows that the stress–-strain curves from the micro tensile tests are consistent with those from the macro tensile tests in the RD. The micro tensions in the TD (Fig. 3b) also exhibit only slightly higher (<10%) flow strengths than the macro tensions and almost identical elongations. The mechanical responses appear substantially anisotropic. Fig. 4 displays the variations of the average strengths and elongations from the micro tensile tests as a function of the angle θ between the loading direction and the lamellar structure. As shown in Fig. 4a, for $\theta = 0°$, both σ_y and σ_{uts} values in the TD ($\sigma_y = 1482 \pm 55$ MPa, $\sigma_{uts} = 1701 \pm 50$ MPa) are higher than those in the RD ($\sigma_y = 1311 \pm 39$ MPa, $\sigma_{uts} = 1437 \pm 34$ MPa), consistent with the

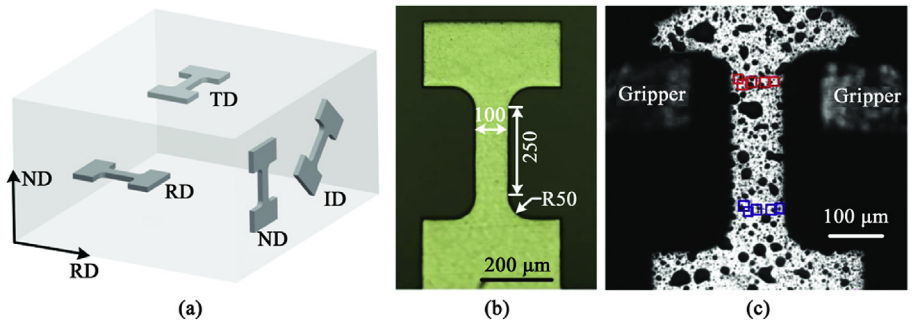

Fig. 1. (a) Schematic of the micro tensile specimens and their orientations in the cold-rolled plate; (b) micro tensile specimen prepared by femtosecond laser machining and electrochemically polishing (numbers indicate the dimensions in micrometers); (c) captured image showing a micro tensile specimen installed in the tungsten gripper. The random black dots in (c) were sprayed intentionally; two groups of pixel subsets were manually selected at both ends of the gauge section to measure strain.

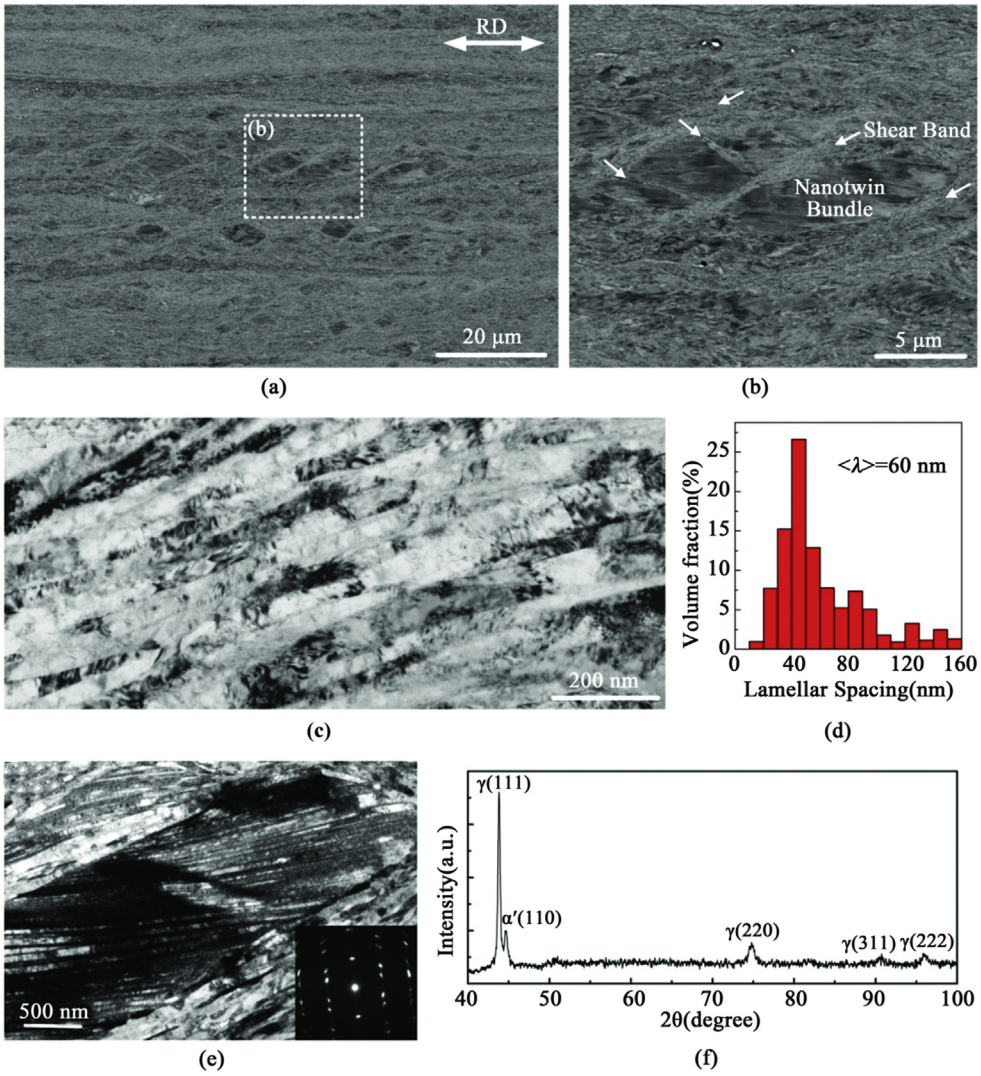

Fig. 2. Cross-sectional microstructure of cold-rolled 316L SS inspected along TD. (a) Overall SEM observations showing the microstructural heterogeneity; (b) bundles of deformation nanotwins cut by localized shear bands (indicated by arrows); (c) TEM micrograph showing the lamellar structure with extended boundaries almost parallel to RD; (d) histogram of lamellar thickness for the lamellar structures; (e) TEM micrograph of a deformation nanotwin bundle (inset is the selected area diffraction pattern); (f) XRD profile showing the presence of major γ austenite phase and minor α' martensite phase.

findings of previous investigators [26]. The σ_y value dramatically decreases to 961 ± 52 MPa for $\theta = 45°$ (ID), and to 931 ± 36 MPa for $\theta = 90°$ (ND). The σ_{uts} value (1218 ± 29 MPa) with $\theta = 45°$ is also much smaller than those at $\theta = 0°$ (RD and TD) but increases again to 1409 ± 21 MPa for $\theta = 90°$ (ND).

The uniform elongation, δ_u, is around 2% for tensions in the RD and TD, characteristic of severely deformed metals. Fig. 4b demonstrates that δ_u increases slightly to ≈4% for $\theta > 45°$, whereas the post-necking elongation $\delta_{pn} = \delta_f - \delta_u$ decreases linearly with increasing θ. This suggests that the post-necking tensile behavior is more greatly orientation dependent. After the initiation of necking, the stress decreases slightly in a stable manner until a $-\delta_{pn}$ of 16% and 11% is achieved in the RD and TD, respectively. In the ID, there is no immediate decrease in stress after necking initiation, followed by a fast stress reduction and eventual fracture (Fig. 3d) with a δ_{pn} of 8.6%, but in the ND the stress is reduced rapidly after necking and δ_{pn} is lowered to ~5% (Fig. 3c).

3.3. Fractographic examination

Fig. 5 shows the fracture surfaces of the macro specimens in the RD

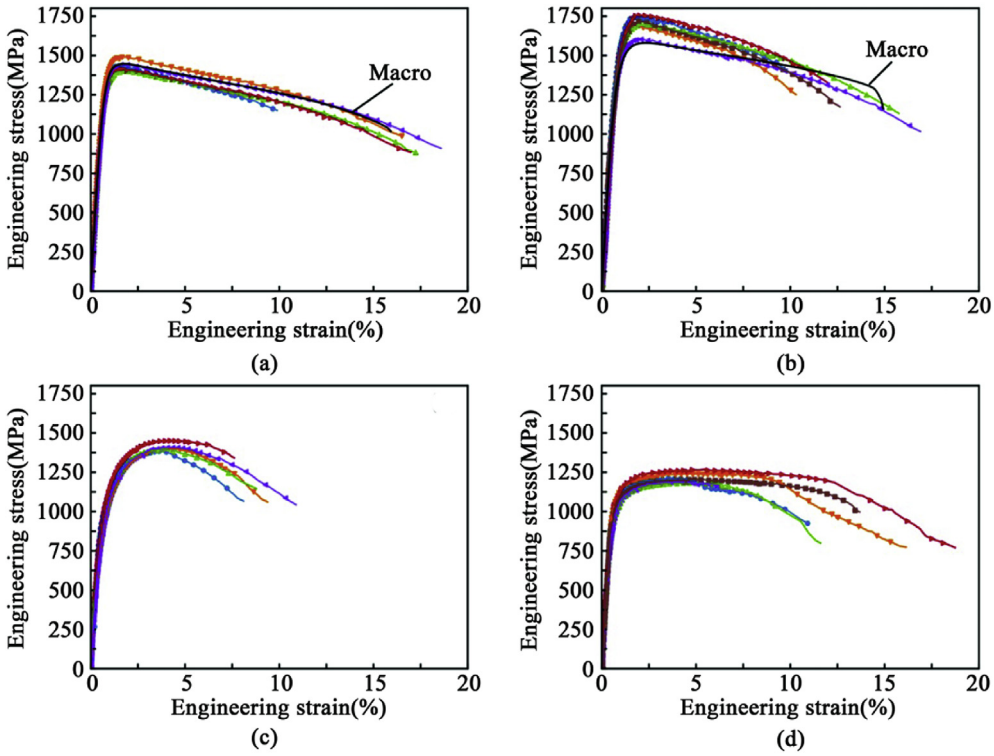

Fig. 3. Engineering stress – strain curves for the micro-tensile tests in (a) RD, (b) TD, (c) ND, (d) ID. The black solid lines without symbols in (a) and (b) are results for the macro-tensile tests.

Table 2
Tensile properties of the cold-rolled 316L stainless steel tested in different directions. σ_y, 0.2% offset yield strength; σ_{uts}, ultimate tensile strength; δ_u, uniform elongation; δ_f, fracture elongation; δ_{pn}, post-necking elongation.

Direction	Specimen	σ_y (MPa)	σ_{uts} (MPa)	δ_u (%)	δ_f (%)	δ_{pn} (%)
RD	Macro	1287 ± 54	1439 ± 37	2.1 ± 0.1	16.2 ± 1.1	14.2 ± 1.0
RD	Micro	1311 ± 39	1437 ± 34	1.7 ± 0.1	17.3 ± 0.8	15.6 ± 0.8
TD	Macro	1340 ± 11	1587 ± 14	2.3 ± 0.1	12.9 ± 0.7	10.6 ± 0.8
TD	Micro	1482 ± 55	1701 ± 50	2.1 ± 0.2	13.0 ± 2.5	11.0 ± 2.4
ND	Micro	931 ± 36	1409 ± 21	3.9 ± 0.2	9.0 ± 1.1	5.1 ± 1.2
ID	Micro	961 ± 52	1218 ± 29	4.2 ± 0.8	12.9 ± 4.0	8.6 ± 3.7

and TD. In the specimen centers, there are evident delamination fractures parallel to the lamellar structures in both tensile directions. The delamination cracks in the RD (Fig. 5b) are much deeper than those in the TD (Fig. 5d). This suggests that the delamination fracture develops more readily in the RD, probably a direct consequence of greater microstructural alignment for the RD than for the TD. There are also numerous fine dimples arising between these large delamination cracks from the final abrupt rupture.

Fig. 6 displays the overall fracture surfaces of the micro tensile specimens tested in directions different from the lamellar structures. Fig. 6 indicates that the tensile direction significantly impacts the failure mode. The RD and TD tensions, parallel to the lamellar structure, exhibit similar failure in a shear mode along an inclined plane after substantial diffuse necking (Fig. 6a and b). Magnified examinations on the fracture surface (Fig. 7a and b) reveal that there are only extremely fine and shallow dimples on the smooth fracture planes. The delamination fracture, as observed in the macro specimens (Fig. 5), does not take place when the specimen size is reduced to the microscale. When tensile loading is perpendicular to the lamellar structure (ND), the necking becomes much more localized (Fig. 6c). Fig. 7c shows that the fracture surface becomes rather undulated and that there are numerous ductile dimples of various sizes. Although the fine dimples are generated by the final fracture, the coarse and deep ones probably form early then grow in size during the tensile deformation. For ID, in which tensile direction is inclined to the lamellar structure, the specimen clearly fractured in a zig-zag manner (Figs. 6d and 7d). The zig-zag morphology evidently develops via nucleating shear fracture cracks along two different lamellar boundaries, which then interconnect by trans-lamellar shearing in another direction.

4. Discussion

4.1. Specimen size effect

It is well known that the flow strength of a material is strongly dependent on the specimen size and geometry [40–42]. In particular, the tendency that “smaller is stronger” has often been seen in specimens of size less than 10 μm [23,42,43], which usually causes ambiguity regarding whether the mechanical properties obtained via micro-scale tests are representative of those of the bulk materials. However, we found that our micro-mechanical experiments produce tensile properties that are specimen size independent compared with those from the corresponding macro tensile tests. The stress−strain curves of the micro and macro tensile tests in the RD entirely coincide, indicating that not

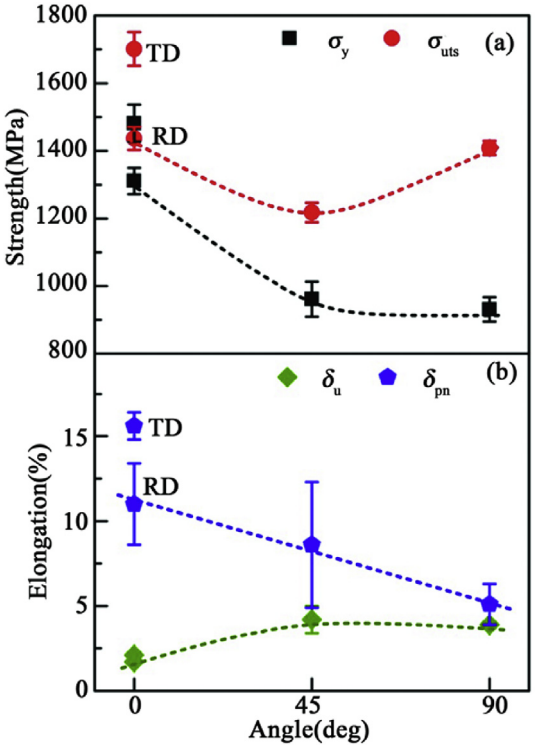

Fig. 4. Variations of the mechanical properties of cold-rolled 316L SS as a function of the angle between the tensile direction and the lamellar interfaces. (a) yield strenth σ_y and ultimate tensile strength σ_{uts}; (b) uniform elongation δ_u and post-necking elongation, δ_{pn}.

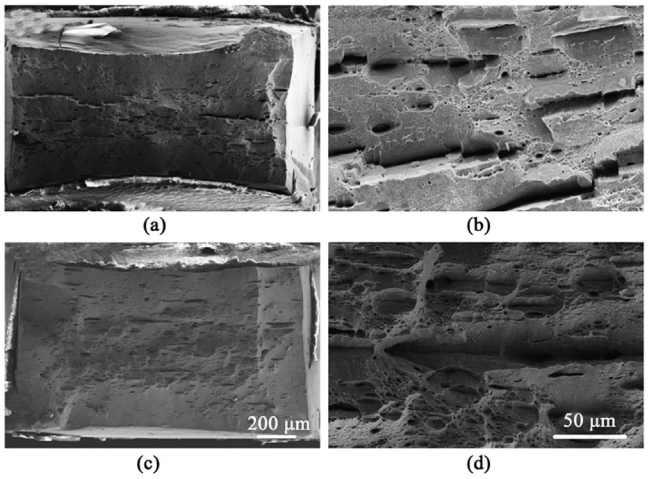

Fig. 5. Fracture surfaces of the macro-tensile specimens tested in the (a, b) RD and (c, d) TD.

only the flow strength and uniform strain but also the non-uniform post-necking ductility can be duplicated in such small specimens. The micro tension in the TD exhibits only marginally higher (<10%) tensile strength and slightly faster stress reduction after the necking compared with the corresponding macro tensile test. This minor specimen size dependence may be the result of the following three aspects: 1) the geometry of the micro specimen is proportionally scaled down from the macro version, eliminating the potential influence of specimen geometry; 2) the thickness of the micro specimen is about 50 μm, much larger than the scale (below 10 μm) where strong size-effect is present [23]; and, 3) taking account of the ultra-fine lamellar structures (<50 nm), there are in fact thousands of lamellae within the gauge sections of the micro specimens thus the internal microstructural effect is much more significant than the specimen surface effect [41]. Based on these considerations, our results suggest that the mechanical properties obtained via the micro tensile tests can well represent the behavior at the macro level.

4.2. *Effect of strain path change*

The stress−strain curves in ND and ID exhibit substantial rounding in the elastic-plastic transition stage, suggesting a reduced yield strength and elevated initial strain hardening. The increase in strain hardening contributes to the greater uniform elongations in these two directions. This phenomenon results from the transient elastic-plastic deformation associated with the effect of strain path change [44–46]. During the cold rolling process, heterogeneous lamellar microstructures gradually develop with strong layers of deformation twins and martensites embedded in the soft matrix of extremely elongated grains. The compressive deformation in the ND during rolling stimulates a pile-up of geometrical necessary dislocations against the boundaries of the hard and soft lamellae. As a consequence, there exists significant internal back stress. The strain direction is reversed under the tension in the ND and ID. The developed internal stress then becomes a driving force for dislocation motion, producing a significantly lessened yield stress. However, given the limited spacing between the lamellar boundaries, the dislocation pile-up re-builds quickly in the opposite interfaces with less tension, thereby resulting in pronounced and rapidly diminished strain hardening during the transient deformation stage.

4.3. *Anisotropic flow strength*

The plastic anisotropy of rolled materials is a well-known and extensively investigated phenomenon. To account for the mechanical anisotropy, both the directionality of deformation induced planar boundaries and the crystallographic texture should be considered [17, 47]. Chowdhury et al. [34] have investigated the microstructural and texture evolution of 316L SS subjected to cold rolling at room temperature. At a thickness reduction of 90%, slightly larger than that (~85%) which we achieved, the steel has one prominent texture component, namely that the brass $\{1\ 1\ 0\}\langle 1\ 1\ 2\rangle$ is anisotropic with a scatter towards the Goss $\{1\ 1\ 0\}\langle 0\ 0\ 1\rangle$ [34]. Moreover, a $\{1\ 1\ 1\}\langle u\ v\ w\rangle$ fibre component is also present, related to the nanotwin regions with TBs which are

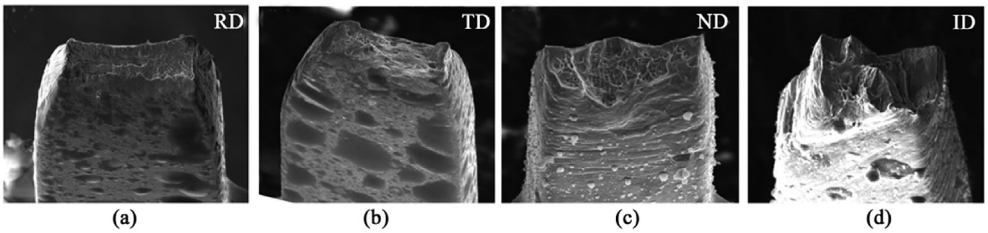

Fig. 6. Overall fracture morphologies of the micro-specimens tested in (a) RD, (b) TD, (c) ND, and (d) ID.

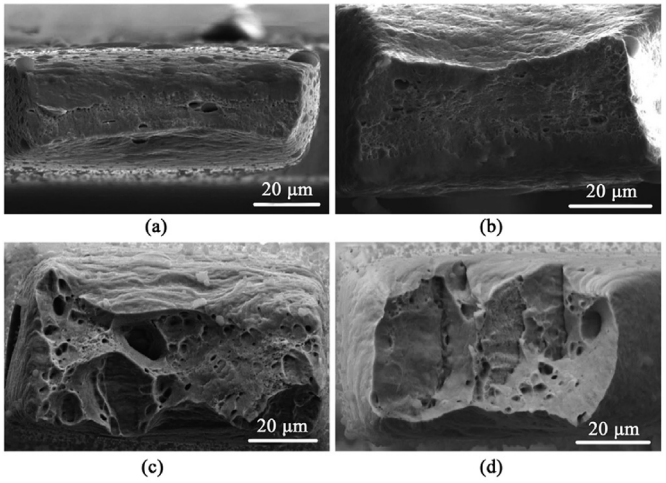

Fig. 7. Fracture surfaces of the micro-tensile specimens tested in (a) RD, (b) TD, (c) ND, and (d) ID.

rotated nearly parallel to the rolling plane [34].

To estimate the orientation dependence of the flow strength for the severely cold-rolled SS, the anisotropic strengthening effect of the extended planar boundaries should be incorporated into the critical resolved shear stress (CRSS) [17]:

$$\tau_{CRSS,i} = \tau_0 + \tau_d + k_{GB} d_i^{-1/2} \quad (1)$$

where τ_0 is the friction stress at undeformed state, k_{GB} is the Hall-Petch coefficient characterizing the strength of grain boundaries (GBs), and d_i is the boundary spacing experienced by the ith slip system. The τ_d term is included to describe the strengthening produced by the dislocations inside the lamellae. Both τ_0 and τ_d are assumed to be common to all slip systems; τ_d is computated as:

$$\tau_d = \alpha \mu b \rho^{1/2} \quad (2)$$

where μ (= 78 GPa) is the shear modulus of the 316L SS, b (= 0.258 nm) is the Burgers vector, α (= 0.5) is a material constant, and ρ is the total dislocation density.

As schematically illustrated in Fig. 8, the dislocation pile-up length d_i is calculated as the distance in the slip plane between the lamellar boundaries [17]:

$$\psi = \arccos(|\mathbf{n}_{LB} \cdot \mathbf{n}_{SP}|) \quad (3)$$

$$d_{SP,i} = \frac{\lambda}{\sin \psi} \quad (4)$$

where λ is the mean lamellar spacing, and $\mathbf{n}_{LB}$ and $\mathbf{n}_{SP}$ are unit vectors

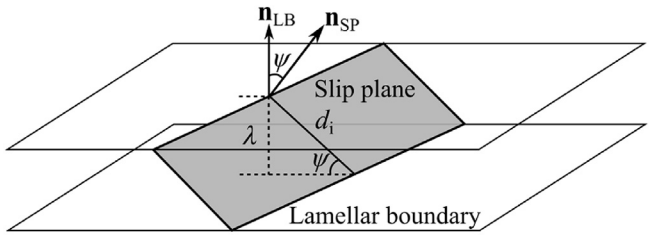

Fig. 8. Schematic illustration of a slip plane intersecting the lamellar boundaries. $\mathbf{n}_{LB}$ and $\mathbf{n}_{SP}$ are unit vectors normal to the lamellar boundary and the slip plane, respectively, ψ is the angle between $\mathbf{n}_{LB}$ and $\mathbf{n}_{SP}$, λ is the lamellar thickness, and d_i is the dislocation pile-up length (assumed to be the distance in the slip plane between the lamellar boundaries).

Table 3
Calculated flow strengths for the three major texture components in different stress directions.

Texture component	Flow strength (MPa)			
	RD	TD	ND	ID
Brass {1 1 0}⟨1 1 2⟩	1454	1789	1789	1332
Goss {1 1 0}⟨0 0 1⟩	1207	1833	1789	1185
{1 1 1}⟨*uvw*⟩ Fiber	1776	1774	2082	1332

normal to the lamellar boundary and to the slip plane, respectively.

By incorporating Eq. (1) into the conventional Taylor model and assuming a uniaxial tensile deformation gradient, the flow strengths for the major texture components in different stressing directions can be computed with τ_0 = 60 MPa, k_{GB} = 1160 MPa nm$^{1/2}$, and with $\rho = 10^{15}$ m^{-2}, a dislocation density typical for severely deformed metals. For the {1 1 1} fiber texture associated with the remained nanotwins, the average TB spacing (30 nm) is taken as λ in Eq. (3), and the flow strength is the mean value for all the crystallographic orientations belonging to the ideal {1 1 1} fiber texture. Table 3 summarizes the calculated results, which should represent the σ_y values in tension. However, due to the aforementioned strain path effect and evident elastic-plastic transient behavior, the experimental σ_y values are significantly reduced in the ND and ID. We therefore compare the modeling results to the σ_{UTS} values. The latter should be only slightly larger than the σ_y values given the diminished strain hardening in extensively deformed metals without strain path effect (as exhibited in the RD). Among the three texture components, the computed flow strengths of the brass texture in the RD, TD and ID are most consistent with the corresponding experimental σ_{UTS} values in the order of TD > RD > ID. This is in agreement with the observation that brass is the dominant texture [34], and suggests that the flow stress anisotropy in these directions is principally a consequence of the existing texture and the lamellar structures. By contrast, our model predicts that the flow strength in the ND should be highest among the testing directions, unlike the experimental ND σ_{UTS}, which is smaller than the TD σ_{UTS}. This inconsistency is probably related to premature tensile failure, as discussed below.

4.4. Orientation dependence of tensile fracture

The fracture surfaces clearly demonstrate that the tensile direction has a strong effect on the fracture behavior that is intimately related to the spatial alignment of the internal lamellar boundaries. The boundaries at the nanometer scale are potential locations of micro-void nucleation [48–50], and the susceptibility of a boundary to void nucleation is enhanced when sharp mechanical variation exists on both sides of the boundary. For the heterogeneous nano-lamellar 316L SS, such discordant boundaries are not hard to find even within the gauge section of the micro specimen, where high strength nanotwin lamellae and elongated martensites are possible hard lamellae adjacent to soft austenitic lamellae. If the tensile direction is parallel to the lamellar structure, the hard and soft lamellae are loaded in parallel fashion (i.e., equally strained), and the stress is locally redistributed (higher stress in the hard regions). Since the strain is compatible, the hard and soft lamellae deform together without failure along the boundary, until eventual trans-lamellar shear rupture.

However, when the specimen is tensioned normal to the lamellar structures, the hard and soft lamellae are loaded in serial fashion (i.e., equally stressed), and the strain is localized and larger in the soft lamellae than in the hard lamellae. The strain incompatibility which gradually develops in the vicinity of the boundary eventually triggers the nucleation and growth of micro-void (see Fig. 7c). Considering our experimental σ_{UTS}, which were smaller than the flow strength we computed for the ND, the micro-void nucleation and growth likely control the premature necking and thus we could not achieve the full flow strength. For

the case in which tensile direction was highly inclined to the lamellar structures, the maximum resolved shear stress is on the planar boundaries, which stimulates concentrated shear parallel to the lamellae. In this stress condition, the hard lamellae exert little restriction on the continuous shear, thus shear cracking eventually occurs along the boundary, as shown in Fig. 7d.

5. Conclusions

We investigated the influence of the lamellae orientation on the mechanical response of 316L SS with heterogeneous nano-lamellar structures using micro-scale tensile experiments in directions parallel, normal, and 45° inclined to the nano-lamellae. We showed that the micro specimens produced size independent mechanical properties similar to those obtainable from macro specimens. The parallel orientation shows the highest strength and smallest uniform elongation, while the inclined orientation exhibits the lowest tensile strength. The normal and inclined orientations exhibit substantially reduced yield strength and pronounced strain hardening, which is a consequence of directional back stress developing in the heterogeneous microstructure. The mechanical anisotropy is well explained given the crystallographic texture and orientation dependent strengthening of the planar boundaries; the exception is the ND, in which the lower strength probably arises from premature tensile failure.

Acknowledgments

The authors acknowledge financial support from the National Key R&D Program of China (Grant No. 2017YFA0204403). L.L. acknowledges financial support by the National Natural Science Foundation of China (Grant No. 51931010, 51601196 and U1608257), the Liaoning Revitalization Talents Program (Grant No. XLYC1802026) and the Key Research Program of Frontier Science, Chinese Academy of Sciences. S.Q. acknowledges the financial support of the Postgraduate Research & Practice Innovation Program of Jiangsu Province (Grant No. KYCX180408). The authors greatly appreciate the assistance of Jiansheng Li in the cold rolling process.

References

[1] X.C. Liu, H.W. Zhang, K. Lu, Strain-induced ultrahard and ultrastable nanolaminated structure in nickel, Science 342 (2013) 337–340.
[2] M. Koyama, Z. Zhang, M. Wang, D. Ponge, D. Raabe, K. Tsuzaki, H. Noguchi, C.C. Tasan, Bone-like crack resistance in hierarchical metastable nanolaminate steels, Science 355 (2017) 1055–1057.
[3] X. Wu, M. Yang, F. Yuan, G. Wu, Y. Wei, X. Huang, Y. Zhu, Heterogeneous lamella structure unites ultrafine-grain strength with coarse-grain ductility, P. Natl. Acad. Sci. USA 112 (2015) 14501–14505.
[4] I.J. Beyerlein, A. Caro, M.J. Demkowicz, N.A. Mara, A. Misra, B.P. Uberuaga, Radiation damage tolerant nanomaterials, Mater. Today 16 (2013) 443–449.
[5] A. Misra, J.P. Hirth, R.G. Hoagland, Length-scale-dependent deformation mechanisms in incoherent metallic multilayered composites, Acta Mater. 53 (2005) 4817–4824.
[6] H.W. Zhang, X. Huang, N. Hansen, Evolution of microstructural parameters and flow stresses toward limits in nickel deformed to ultra-high strains, Acta Mater. 56 (2008) 5451–5465.
[7] L.F. Zeng, R. Gao, Q.F. Fang, X.P. Wang, Z.M. Xie, S. Miao, T. Hao, T. Zhang, High strength and thermal stability of bulk Cu/Ta nanolamellar multilayers fabricated by cross accumulative roll bonding, Acta Mater. 110 (2016) 341–351.
[8] S.J. Zheng, J. Wang, J.S. Carpenter, W.M. Mook, P.O. Dickerson, N.A. Mara, I.J. Beyerlein, Plastic instability mechanisms in bimetallic nanolayered composites, Acta Mater. 79 (2014) 282–291.
[9] N. Tsuji, R. Ueji, Y. Minamino, Y. Saito, A new and simple process to obtain nanostructured bulk low-carbon steel with superior mechanical property, Scripta Mater. 46 (2002) 305–310.
[10] F. Liu, H. Yuan, S. Goel, Y. Liu, J.T. Wang, Bulk nanolaminated nickel: preparation, microstructure, mechanical property, and thermal stability, Metall. Mater. Trans. A 49 (2018) 576–594.
[11] X.C. Liu, H.W. Zhang, K. Lu, Formation of nanolaminated structure in an interstitial-free steel, Scripta Mater. 95 (2015) 54–57.
[12] Z. You, X. Li, L. Gui, Q. Lu, T. Zhu, H. Gao, L. Lu, Plastic anisotropy and associated deformation mechanisms in nanotwinned metals, Acta Mater. 61 (2013) 217–227.
[13] Y.P. Li, G.P. Zhang, W. Wang, J. Tan, S.J. Zhu, On interface strengthening ability in metallic multilayers, Scripta Mater. 57 (2007) 117–120.
[14] M. Dupeux, F. Durand, Anisotropic tensile properties of a lamellar Al-CuAl2 eutectic composite, Metall. Trans. A 6 (1975) 2143–2151.
[15] P. Ghosh, K.S. Kormout, U. Lienert, J. Keckes, R. Pippan, Deformation characteristics of ultrafine grained and nanocrystalline iron and pearlitic steel - an in situ synchrotron investigation, Acta Mater. 160 (2018) 22–33.
[16] T. Nizolek, I.J. Beyerlein, N.A. Mara, J.T. Avallone, T.M. Pollock, Tensile behavior and flow stress anisotropy of accumulative roll bonded Cu-Nb nanolaminates, Appl. Phys. Lett. 108 (2016), 051903.
[17] Z.J. Li, G. Winther, N. Hansen, Anisotropy in rolled metals induced by dislocation structure, Acta Mater. 54 (2006) 401–410.
[18] D. Juul Jensen, N. Hansen, Flow stress anisotropy in aluminium, Acta Metall. Mater. 38 (1990) 1369–1380.
[19] C.R. Mayer, L.W. Yang, S.S. Singh, J. Llorca, J.M. Molina-Aldareguia, Y.L. Shen, N. Chawla, Anisotropy, size, and aspect ratio effects on micropillar compression of AlSiC nanolaminate composites, Acta Mater. 114 (2016) 25–32.
[20] M.W. Kapp, A. Hohenwarter, S. Wurster, B. Yang, R. Pippan, Anisotropic deformation characteristics of an ultrafine- and nanolamellar pearlitic steel, Acta Mater. 106 (2016) 239–248.
[21] A.J. Palomares-García, M.T. Pérez-Prado, J.M. Molina-Aldareguia, Effect of lamellar orientation on the strength and operating deformation mechanisms of fully lamellar TiAl alloys determined by micropillar compression, Acta Mater. 123 (2017) 102–114.
[22] W.D. Nix, H. Gao, Indentation size effects in crystalline materials: a law for strain gradient plasticity, J. Mech. Phys. Solid. 46 (1998) 411–425.
[23] M.D. Uchic, P.A. Shade, D.M. Dimiduk, Plasticity of micrometer-scale single crystals in compression, Annu. Rev. Mater. Res. 39 (2009) 361–386.
[24] Q.Y. Long, J.X. Lu, T.H. Fang, Microstructure and mechanical properties of AISI 316L steel with an inverse gradient nanostructure fabricated by electro-magnetic induction heating, Mater. Sci. Eng., A 751 (2019) 42–50.
[25] J. Li, Y. Cao, B. Gao, Y. Li, Y. Zhu, Superior strength and ductility of 316L stainless steel with heterogeneous lamella structure, J. Mater. Sci. 53 (2018) 10442–10456.
[26] H. Miura, M. Kobayashi, Y. Todaka, C. Watanabe, Y. Aoyagi, N. Sugiura, N. Yoshinaga, Heterogeneous nanostructure developed in heavily cold-rolled stainless steels and the specific mechanical properties, Scripta Mater. 133 (2017) 33–36.
[27] A. Belyakov, M. Odnobokova, A. Kipelova, K. Tsuzaki, R. Kaibyshev, Microstructural evolution and strengthening of stainless steels during cold rolling, in: M. Muruganant, Chirazi Ali, Baldev Raj (Eds.), Frontiers in Materials Processing, Applications, Research and Technology, Springer Singapore, Singapore, 2018, pp. 341–347.
[28] M.J. Pfeifenberger, M. Mangang, S. Wurster, J. Reiser, A. Hohenwarter, W. Pfleging, D. Kiener, R. Pippan, The use of femtosecond laser ablation as a novel tool for rapid micro-mechanical sample preparation, Mater. Des. 121 (2017) 109–118.
[29] S.K. Slaughter, J.P. Ligda, T. Sano, B.E. Schuster, High throughput femtosecond-laser machining of micro-tension specimens, in: TMS 2015 144th Annual Meeting & Exhibition, Springer International Publishing, Cham, 2016, pp. 471–478.
[30] M.P. Echlin, M.S. Titus, M. Straw, P. Gumbsch, T.M. Pollock, Materials response to glancing incidence femtosecond laser ablation, Acta Mater. 124 (2017) 37–46.
[31] D.J. Magagnosc, J.P. Ligda, T. Sano, B.E. Schuster, Femtosecond laser machining of micro-tensile specimens for high throughput mechanical testing, in: La Vern Starman, Jenny Hay (Eds.), Micro and Nanomechanics vol. 5, Springer International Publishing, Cham, 2018, pp. 7–9.
[32] Z. You, S. Qu, S. Luo, L. Lu, Fracture toughness evaluation of nanostructured metals via a contactless crack opening displacement gauge, Materialia 7 (2019), 100430.
[33] H. Wang, Z. You, L. Lu, Kinematic and isotropic strain hardening in copper with highly aligned nanoscale twins, Mater. Res. Lett. 6 (2018) 333–338.
[34] S.G. Chowdhury, S. Das, P.K. De, Cold rolling behaviour and textural evolution in AISI 316L austenitic stainless steel, Acta Mater. 53 (2005) 3951–3959.
[35] G.Z. Liu, N.R. Tao, K. Lu, 316L austenite stainless steels strengthened by means of nano-scale twins, J. Mater. Sci. Technol. 26 (2010) 289–292.
[36] N.R. Tao, K. Lu, Nanoscale structural refinement via deformation twinning in face-centered cubic metals, Scripta Mater. 60 (2009) 1039–1043.
[37] F.K. Yan, G.Z. Liu, N.R. Tao, K. Lu, Strength and ductility of 316L austenitic stainless steel strengthened by nano-scale twin bundles, Acta Mater. 60 (2012) 1059–1071.
[38] N. Nakada, H. Ito, Y. Matsuoka, T. Tsuchiyama, S. Takaki, Deformation-induced martensitic transformation behavior in cold-rolled and cold-drawn type 316 stainless steels, Acta Mater. 58 (2010) 895–903.
[39] M. Eskandari, A. Najafizadeh, A. Kermanpur, Effect of strain-induced martensite on the formation of nanocrystalline 316L stainless steel after cold rolling and annealing, Mater. Sci. Eng., A 519 (2009) 46–50.
[40] Y.H. Zhao, Y.Z. Guo, Q. Wei, A.M. Dangelewicz, C. Xu, Y.T. Zhu, T.G. Langdon, Y.Z. Zhou, E.J. Lavernia, Influence of specimen dimensions on the tensile behavior of ultrafine-grained Cu, Scripta Mater. 59 (2008) 627–630.
[41] L. Yang, L. Lu, The influence of sample thickness on the tensile properties of pure Cu with different grain sizes, Scripta Mater. 69 (2013) 242–245.
[42] J.R. Greer, J.T.M. De Hosson, Plasticity in small-sized metallic systems: intrinsic versus extrinsic size effect, Prog. Mater. Sci. 56 (2011) 654–724.
[43] D. Kiener, P. Hosemann, S.A. Maloy, A.M. Minor, In situ nanocompression testing of irradiated copper, Nat. Mater. 10 (2011) 608–613.
[44] D.V. Wilson, P.S. Bate, Influences of cell walls and grain boundaries on transient responses of an if steel to changes in strain path, Acta Metall. Mater. 42 (1994) 1099–1111.
[45] F. Li, P.S. Bate, Strain path change effects in cube textured aluminium sheet, Acta Metall. Mater. 39 (1991) 2639–2650.
[46] M. Zandrahimi, S. Platias, D. Frice, D. Barrett, P.S. Bate, W.T. Roberts, Effects of changes in strain path on work hardening in cubic metals, Metall. Trans. A 20 (1989) 2471–2482.

[47] G. Winther, Effect of grain orientation dependent microstructures on flow stress anisotropy modelling, Scripta Mater. 52 (2005) 995–1000.
[48] K.S. Kumar, H. Van Swygenhoven, S. Suresh, Mechanical behavior of nanocrystalline metals and alloys, Acta Mater. 51 (2003) 5743–5774.
[49] R. Pippan, A. Hohenwarter, The importance of fracture toughness in ultrafine and nanocrystalline bulk materials, Mater. Res. Lett. 4 (2016) 127–136.
[50] A. Pineau, A. Amine Benzerga, T. Pardoen, Failure of metals III: fracture and fatigue of nanostructured metallic materials, Acta Mater. 107 (2016) 508–544.